J. Fluid Mech. (2014), *vol.* 739, *pp.* 338–362. © Cambridge University Press 2013
doi:10.1017/jfm.2013.611

Experimental study of a model valve with flexible leaflets in a pulsatile flow

R. Ledesma-Alonso, J. E. V. Guzmán and R. Zenit†

Instituto de Investigaciones en Materiales, Universidad Nacional Autónoma de México, Apdo. Postal 70-360, México D.F. 04510, México

(Received 26 June 2012; revised 28 August 2013; accepted 13 November 2013; first published online 18 December 2013)

An experimental investigation was conducted to study the dynamical behaviour of a model valve in a pulsatile flow. The valve is modelled as a pair of curved, rectangular, flexible leaflets that open and close under a time-periodic flow. Using image analysis, the range of flow parameters for which a valve (of a particular geometry and material properties of the leaflets) works correctly were identified. A correct performance was considered to be when the valve opened in one direction but blocked the flow in the reversed direction. A model is proposed to predict the performance of the valves. Furthermore, an analysis of fluid strains is conducted for valves that operate correctly to identify the influence of the valve's design on fluid stresses. The main purpose of this investigation is to gain insight for the design of future prosthetic heart valves.

Key words: biological fluid dynamics, biomedical flows

1. Introduction

Four valves in the interior of the human heart keep the blood flowing in one direction, preventing backflows when reversed pressure gradients occur. For example, during the cardiac systolic phase the blood is ejected from the left ventricle through the aortic valve, while the mitral valve remains closed to impede a flow into the corresponding atrium. When any of these valves fails to work properly, or exhibits some kind of pathology, it usually has to be replaced by a prosthetic heart valve. Although a large variety of models are currently available, Yoganathan, He & Casey-Jones (2004) have shown that biological prosthesis have excellent mechanical and haemodynamic properties. Biological prosthesis can either be valves taken from animals (usually porcine), or be constructed to resemble the original ones but using biological materials (such as bovine pericardium). Owing to their resemblance to native valves, this type of prothesis produces a central fluid jet which reduces its thrombogenic potential and minimizes the transvalvular pressure drop. However, the natural tissues constituting the valve's leaflets may sustain severe outwear, overgrowth and calcification, leading to a considerably shorter durability. In contrast, mechanical prostheses have longer lifespan and minimize backflow, but they also generate inadequate physiological flow conditions (i.e. high stress levels in the blood (Lopez-Zazueta *et al.* 2011)). In general, these conditions encompass effects such as stagnation, cavitation, haemolysis, and thrombus formation (at the hinges and pivots),

† Email address for correspondence: zenit@unam.mx

https://doi.org/10.1017/jfm.2013.611 Published online by Cambridge University Press

and therefore entail the problem of lifelong anticoagulation treatments (Yoganathan *et al.* 2004).

Today, improvements to the valve designs are being guided by a considerable amount of theoretical and experimental research. The emphasis has been placed on the evaluation of new bio-compatible materials (Bernacca *et al.* 2002; Jamieson 2002), and on the particular fluid-mechanical aspects of the transvalvular flows that lead to blood damaging processes (Lim *et al.* 2001; Schneider *et al.* 2007). Owing to the complexity of the problem, the effects produced by specific parameters are usually studied through a series of simplified problems. As a result, the analysis of the coupled interaction between leaflets and pulsatile flows has become an attractive topic that has been addressed in different ways in recent investigations. For example, the experimental work by Leo *et al.* (2006) was aimed at understanding the effects produced on the flow by parameters such as the thickness of the leaflets and the commissural design (i.e. the boundaries of attachment between leaflets). The authors conducted three-dimensional particle image velocimetry (PIV) measurements on polyurethane trileaflet valves with aortic-like flow conditions and quantitatively described those effects. The three-lobed velocity profiles formed downstream were observed to depend on commissural design, and it was also argued that the leakage was directly related to the thickness of the leaflets.

In a more theoretical approach, de Hart *et al.* (2000) and Stijnen *et al.* (2004) considered the whole fluid–structure problem and studied the behaviour of (single) flexible and stiff leaflets under pulsatile flow conditions. The problem was further complicated by reproducing a sinus cavity inside the rectangular test channel. To this end, the authors implemented and validated the fictitious domain method (FDM) but without discussing any design criteria. Watton *et al.* (2006) implemented the immersed boundary method (IBM) instead, to analyse the large deformations of the leaflets during their interaction with the flow. The behaviour of different valve types was studied for a range of physiological-like flows with the objective of aiding the design process. Some recently developed polyurethane prosthetic valves, whose geometry and material properties were based on those of the native mitral valve, were tested as well. Pedrizzetti & Domenichini (2006) investigated the dynamics of a flow within a two-dimensional channel, initially closed by a rigid 'inertialess' mobile leaflet, by means of a coupled numerical solution for the flow and the solid. The main interests were the vortex formation at the free edge of the single leaflet (of fixed thickness and length) and its corresponding shedding process. The authors maintained that a basic model could capture the general features of transvalvular flows and, moreover, that the analysis of the flow-driven opening of the leaflets was a necessary step towards understanding the full dynamical problem of real valves.

Additional research concerning the properties of the materials was conducted by Prot, Skallerud & Holzapfel (2007), who simulated the mitral apparatus with several biological membrane models. Essential features of the soft tissues, composed of collagen fibres, were included in the constitutive models to capture the typical stress–strain response of the valves. It was found that the heart tissue exhibits anisotropic and a highly nonlinear stress–strain behaviour. Additionally, the large leaflet deformations observed during the *in vivo* measurements suggested the necessity of employing hyperelastic models, together with the theory of shells to cope with the complex behaviour of the material and the appearance of plane stress states. The investigation conducted by Bernacca *et al.* (2002) sought to determine the effects that the elastic modulus and the thickness had on the hydrodynamic response and the durability of prosthetic trileaflet valves. Their results revealed that the hydrodynamic characteristics of the valves were significantly affected by

https://doi.org/10.1017/jfm.2013.611 Published online by Cambridge University Press

both parameters. Interestingly, however, the leakage and the mean pressure gradients remained within their original orders of magnitude for the range of elastic moduli and thicknesses explored. It was also indicated that variations of the thickness and the elasticity were responsible for the inadequate operation of the valves; more specifically, it was observed that several prostheses could not open all three leaflets at low cardiac outputs.

In view of the previous considerations, the present study was conceived to experimentally survey the fundamental physical processes governing the response of flexible leaflets exposed to periodic flows. We constructed a quasi-two-dimensional arrangement to simplify the problem while preserving the main characteristics intact. Therefore, we consider an arrangement of two rectangular, symmetrical leaflets which work as a valve. Their length is longer than the half-width of the channel; therefore, they are curved in a static configuration when the flow is absent. But, when it is large enough, its action makes the leaflets open, increasing their local curvature.

Optical techniques were used to analyse the flow field in the two-dimensional experimental setup. The main objective was to determine the hydrodynamic performance of rectangular valves in terms of their thickness, d, their length, l, and their (secant) modulus of elasticity, E_s. Emphasis was put on analysing the velocity and the rate-of-strain fields, in view of their intrinsic relation with the haemolysis and thrombogenic processes. As has been pointed out by several authors (e.g. Yoganathan *et al.* 2004; Schneider *et al.* 2007), such fields are also involved in the activation of the platelets and other blood factors (like the von Willebrand factor). Thus, relating the spatial distributions of these fields to the elastic behaviour of the leaflets is an important part of the present analysis.

In the present study a map for the closing performance of each valve type was obtained, from the experimental results, in terms of the flow properties, the geometric characteristics of the leaflets and their material properties. The map is based on the relative importance of the two main forces acting on the leaflets during the closure of the valve: a dynamic force (represented by the pressure exerted over the surface of the leaflets) and the elastic bending force exerted by each leaflet on the other. It was found that the valve will perform its function correctly when the elastic forces are larger than the dynamic ones. Otherwise, the valve fails to perform its basic function and a backward flow occurs.

It is important to emphasize that this investigation is not aimed at exactly mimicking the flows through native heart valves (and their prosthetic counterparts), nor to produce clinical-grade data. Instead, we consider a simplified two-dimensional valve model which retains only the essential flexibility and geometrical properties of leaflets in a pulsatile flow. Our aim is to reveal the basic mechanisms involved in the open–close operation of a flexible leaflet valve. In this manner, the behaviour of the model valve in a pulsatile flow can finally be expressed in terms of the forces concerned in the fluid–structure interaction. In this sense, our two-dimensional model valve serves only as a reference point to guide further research. Although the results obtained from the simplified model are of limited value in the context of real native or prosthetic valves, the associated analysis provides some insights about the true nature of the fluid–structure interaction. Moreover, the relation between the evolution of the flow and the blood damaging processes is considered to be of paramount importance. Hence, the connection between these two aspects of the problem has been underlined in most previous research efforts. In the present case such a context provides our ultimate goal, which is to understand the nature of the blood trauma process in prosthetic devices.

https://doi.org/10.1017/jfm.2013.611 Published online by Cambridge University Press

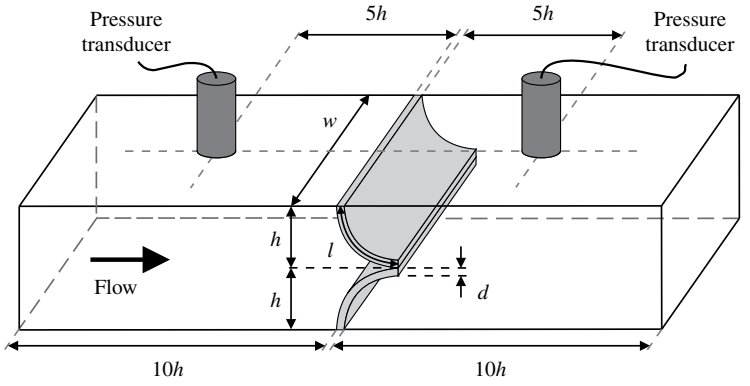


FIGURE 1. Layout of the test section and specimen configuration: h and w indicate the semi-height and width of the test channel, respectively, while l and d express the length and the thickness of the leaflets. The position of the pressure transducers relative to the valve is also shown.

2. Experimental methodology

2.1. *Test apparatus and valve specimens setup*

A flow circuit was built according to the Windkessel model described by Diourté *et al.* (1999). The system is constituted of a pulsatile pump, a compliance chamber, a needle valve, and a test channel with a clamp to hold the leaflets. The ranges of the operating variables (see below) retain some resemblance with those of the human circulatory system.

According to Sherwood (1997), the main parameter in the study of blood flow through the circulatory system is the cardiac output $\langle \dot{G} \rangle$. Equivalent to the average (volume) flow rate, the average cardiac output $\langle \dot{G} \rangle = f\,V$ is given by the pulsation rate f, which is the number of beats per unit time, and the stroke volume V, which is the expelled volume per beat. In medical applications these quantities depend on age, weight, gender, health condition, current physical activity, and the side of the heart being considered. The experiment was set up in such a way that both parameters could be varied independently to produce a set of the outputs within the range of normal human cardiac conditions. A single value of the systolic fraction, t_S, was employed for this study. A positive displacement pump (Harvard Apparatus, model 1423) was installed to establish the pulsatile flow conditions for the experiments. For a fixed systolic–diastolic ratio of 35/65, the frequency and the stroke volume were set such that the average cardiac output could reach a maximum value of $\langle \dot{G} \rangle = 166.7\ \mathrm{cm}^3\ \mathrm{s}^{-1}$. A chamber filled with 5 mm glass spheres was installed at the inlet of the test section in order to make the incoming flow uniform. The test section consisted of a transparent acrylic rectangular box with a cross-section of $2h \times w$ and a length of $20h$, where $h = 15$ mm and $w = 50$ mm are the semi-height and the width of the test channel, respectively. The leaflets were clamped to a specially designed support placed inside the test section $10h$ downstream of the inlet of the chamber. The model valves were composed of twin leaflets situated on opposite sides of the test section such that they were aligned perpendicularly to the walls, as illustrated in figure 1. In all cases the length of each leaflet was longer than the channel semi-height; hence, the two leaflets were curved and met each other at the centre of the channel (approximately at $y = 0$) as also depicted in figure 1. This arrangement

https://doi.org/10.1017/jfm.2013.611 Published online by Cambridge University Press

allowed the leaflets to be easily opened for positive displacements of the fluid (from left to right in the figure). When the pressure gradient changed, the two leaflets closed impeding the backward flow (from right to left). By varying the stroke volume and the frequency, the conditions for which this behaviour was observed were identified. We call this correct performance. In contrast, for certain conditions of cardiac output, leaflet thickness, length and material properties, the reverse pressure gradient was large enough to make the leaflets to buckle and permit a reversed flow. This condition was identified as faulty performance.

Two pressure transducers (Druck PDCR 810) were placed upstream and downstream of the valve at a distance of $5h$ along the centreline of the channel. The corresponding measuring ranges were ± 1.0 bar and ± 0.7 bar, respectively. The typical time response of the transducers was 35 μs, which is much smaller that the characteristic time of any of the experiments conducted here. A compliance chamber was used, at the outlet of the test section, to simulate the elasticity of the circulatory system. During the diastolic phase of the cycle the increased pressure generated inside the cavity favoured the closure of the valve. This compliance chamber was made of a cylindrical acrylic tube with an inner diameter of 140 mm and a height of 230 mm. The compliance tank was set to operate with an initial void fraction of 60 %. The pressure drop in the system was regulated with a needle valve which remained half-opened during all the experiments.

Water was selected as the working fluid for convenience. Its density and viscosity were taken to be $\rho_f = 1000$ kg m^{-3} and $\mu_f = 0.001$ Pa s, respectively. The selection of water was justified on the grounds that blood behaves as a Newtonian fluid in many instances (Sherwood 1997). Its shear-thinning effects would be relevant in small capillary vessels where the size of the blood cells (i.e. erythrocytes, leukocytes and platelets) is comparable to the internal diameter of the conduits or when large velocity gradients appear (Alonso, Pries & Gaehtgens 1993; Barshtein, Wajnblum & Yedgar 2000). The implementation of the PIV technique also required the use of an optically transparent medium. It must be noted that non-Newtonian effects have been reported to affect leakage flows (Pohl *et al.* 1996) and vorticity production (Palacios-Morales & Zenit 2013). To keep the study focused on the valve operation, we opted not to include such effects.

The range of Reynolds numbers ($Re = \langle \dot{G} \rangle \rho_f / (w\mu_f)$) obtained in the experiments are within the same order of magnitude as those reported in the literature. Nevertheless, since the actual size of the model valve is slightly larger than the effective orifice area (EOA) of most prosthetic valves, Re observed in this study is globally lower. It should be remarked that the experimental setup follows the so-called Windkessel design, and that only average quantities of the main flow parameters have been considered.

The model valves were made with twin, rectangular leaflets. Each pair had a unique combination of thickness (d), length (l), density (ρ_s), and secant modulus of elasticity (E_s). The nonlinear elastic behaviour of the materials was captured by characterizing E_s. The corresponding stress–strain curves were determined from series of tensile tests performed on material samples. Details of the procedure to determine the elastic properties of the materials can be found in Ledesma-Alonso (2010). Four commercially available materials were considered: natural latex, silicone rubber, neoprene and aluminium. Their respective properties are shown in table 2 below. The flexural rigidity was calculated as $E_s I$, where the moment of inertia for leaflets with a rectangular cross-section is $I = wd^3/12$. To study a case with high rigidity a set of silicone leaflets was reinforced with aluminium.

https://doi.org/10.1017/jfm.2013.611 Published online by Cambridge University Press

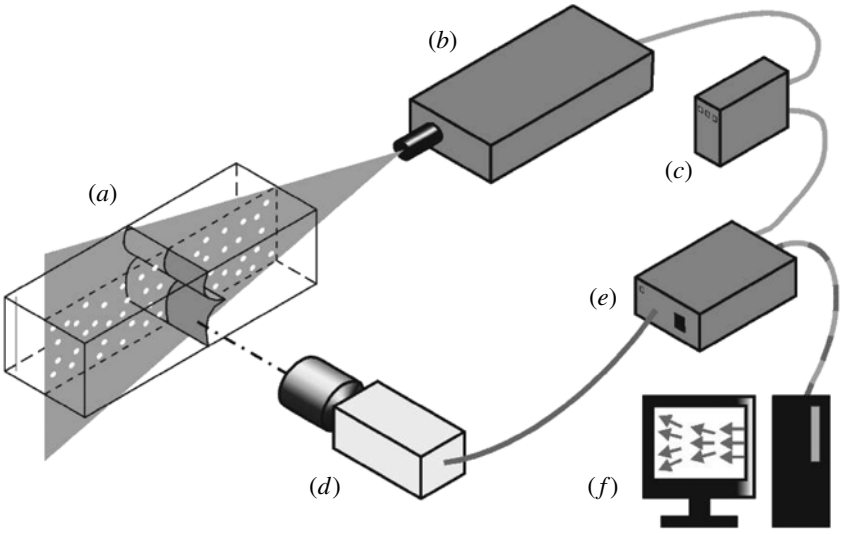


FIGURE 2. PIV system: (*a*) laser sheet with reflecting tracers, (*b*) laser system and optic arrangement, (*c*) laser control device, (*d*) CCD camera with green filter, (*e*) FlowMap processor, (*f*) computer with the FlowManager software.

The operation of the system was triggered by an electrical signal from the pump. The synchronization of all the elements (i.e. pump, lasers, cameras, and acquisition equipment) was performed with a National Instruments DAQ/DAX-6031 card and a LabView code.

2.2. *Video imaging and particle image velocimetry*

A digital camera (Motionscope PCI 8000 s^{-1}) was employed to observe the operation of the leaflets at a rate of 60 frames per second. The proper opening and closing processes were assessed by analysing the image sequences. In addition, the images were used to measure the elongation and the deflection of the leaflets.

A two-dimensional PIV measurement system for the velocity fields was implemented for the experiments. The experimental arrangement of the PIV system is shown schematically in figure 2. Silver-coated glass spheres with a mean diameter of 10 μm and a density of $\rho = 1010$ kg m^{-3} were used as flow tracers. A 532 nm Nd-YAG laser emitted a 50 mJ pulsed laser beam, which was then transformed into a laser sheet with a thickness of 0.5 mm by means of a semi-cylindrical lens. The laser sheet illuminated a single plane in the middle of the test section across the main flow direction. The motion of the illuminated tracer particles was registered with a CCD camera (Kodak Megaplus ES1.0). The camera was placed at the mid-plane of the test channel in a direction perpendicular to the laser sheet. Both laser and camera were synchronized to obtain images. A scale factor of 4.05×10^{-2} mm $pixel^{-1}$ was used. Interrogation areas of 64×64 pixels were defined and consecutive pairs of images were cross-correlated in order to obtain the velocity vectors. An adaptive cross-correlation technique was implemented in regions of the flow where the velocity gradients were the largest. Within this scheme the interrogations windows were reduced from 64×64 pixels to 32×32 pixels (with a 30 % overlap) to yield a spatial resolution of $\sim$1.3 mm $pixel^{-1}$. Vector fields were subjected to standard validation, filtering and smoothing procedures. The concentration of tracer particles was chosen to produce at

https://doi.org/10.1017/jfm.2013.611 Published online by Cambridge University Press

Stroke volume V (10^{-5} m^3)	Frequency f (s^{-1})	Systolic fraction t_S (%)
2.6	0.333	0.35
3.8	0.333 0.666	0.35
5.1	0.333 0.666	0.35

TABLE 1. Parameters corresponding to the experiments for which PIV measurements were performed.

least 10 tracers per interrogation window in order to reduce the noise-to-signal ratio, as well as the particle displacement-to-interrogation window ratio.

To obtain velocity measurements up- and downstream of the leaflets, a mirror was used. The mirror, which was carefully aligned, was placed below the channel to reflect part of the laser sheet and also illuminate the downstream side of the flow.

Table 1 summarizes the flow parameters of the experiments for which the PIV measurements were performed.

Note that the measurements conducted in this investigation are two-dimensional. We can only obtain measurements of the flow velocity in the middle of the test section. Recently Hutchison, Sullivan & Ethier (2011) showed that for the case of a mechanical valve, secondary flows (perpendicular to the main flow direction) are present but their strength is small. Thus we can argue that, although present, the secondary flows do no affect significantly our performance assessment of the model two-dimensional valve. Furthermore, we compared the flow rate calculated from the PIV measurements to that given by the pump ($\langle \dot{G} \rangle = f\,V$), leading to good agreement for most conditions (Ledesma-Alonso 2010).

2.3. *Phase-locking technique and mean flow properties*

The phase-locking technique was implemented to produce synchronized measurements at particular instants of interest within the operating cycle. A total of 250 experimental realizations per time interval allowed the statistical treatment of the signals obtained, simultaneously, from the pressure transducers, the PIV system and camera. Prescribed delays at the beginning of each cycle were used to establish fifteen different time increments during the cycle. The phase-averaged values of the velocity components, which depend on position and time, were calculated as

$$\overline{v_k}(\boldsymbol{x}, \tau) = \frac{1}{N} \sum_{i=0}^{N} v_k(\boldsymbol{x}, t). \tag{2.1}$$

In (2.1), the (Eulerian) position coordinate is represented by $\boldsymbol{x}$ and the 'locked' time by $t = \tau + iT$, where T is the duration of the cycle and τ is a particular time of interest within the interval $0 \leqslant \tau < T$. The sum is taken over the total number of samples, N, acquired at the specified instant τ. The average velocity field (throughout a representative cycle) was spatially reconstructed with statistical (arithmetic mean) and interpolation (cubic spline) schemes.

We verified that the number of experimental realizations was large enough to reach statistical convergence. The mean quantities were calculated with progressively larger

https://doi.org/10.1017/jfm.2013.611 Published online by Cambridge University Press

https://doi.org/10.1017/jfm.2013.611 Published online by Cambridge University Press

Leaflet type		Material	Density ρ_s (kg m^{-3})	Secant modulus E_s (10^6 kg m^{-1} s^2)	Length l (10^{-2} m)	Width w (10^{-2} m)	Thickness d (10^{-4} m)	Flexural rigidity E_sI (10^{-6} kg m^3 s^{-2})
Al1 Al2	□ ■	Aluminum & Silicone	1680	7×10^4	1.50 2.63	5	7.94	1.466×10^5
La	△	Latex	960	0.83	2.63	5	3.97	0.230
Ne	◊	Neoprene	1140	2.96	2.63	5	7.94	6.197
Si1	⊕				2.25			
Si2	•				2.63			
Si3	⊙	Silicone	1070	2.15	3.00	5	3.97	0.595
Si4	⊗				3.38			
Si5	⊘				3.75			
Si	◯	Silicone	1167	2.20	2.63	5	7.94	4.606

TABLE 2. Material and geometrical properties of the leaflets, and symbols used in the figures.

data sets. We found that for 200 realizations or more the average did not vary significantly (below 5 % variation). Clearly, this number of measurements is enough to calculate the mean quantities; higher-order terms would need more measurements. In this investigation we focus only on the mean velocity field and its space gradients, for which the measurements have statistically converged.

Other important properties of the flow were determined from the average velocity field. Of particular interest were the components of the rate-of-strain tensor, since their relative influence is fundamental in the blood damaging processes occurring in flows through artificial heart valves (Giersiepen *et al.* 1990; Hellums 1994; Bluestein, Rambod & Gharib 2000).

According to Whitaker (1981), the rate-of-strain and rotation tensors can be determined from the velocity gradients as

$$\boldsymbol{S} = \tfrac{1}{2}[\nabla \boldsymbol{v} + (\nabla \boldsymbol{v})^{\mathrm{T}}], \tag{2.2}$$

and

$$\boldsymbol{\Omega} = \tfrac{1}{2}[\nabla \boldsymbol{v} - (\nabla \boldsymbol{v})^{\mathrm{T}}]. \tag{2.3}$$

Their corresponding magnitudes can be obtained as

$$|\boldsymbol{S}| = \sqrt{\boldsymbol{S}{:}\boldsymbol{S}^{\mathrm{T}}}, \quad |\boldsymbol{\Omega}| = \sqrt{\boldsymbol{\Omega} : \boldsymbol{\Omega}^{\mathrm{T}}}. \tag{2.4}$$

Note that the calculation of the strain rate values is limited by the spatial resolution of the PIV setup (1.3 mm pixel^{-1}). Therefore, it must be emphasized that the reported results are sufficiently accurate for velocities close to the average values. For peak velocities, however, the corresponding estimates cannot be obtained because a higher resolution is required. The uncertainty of our measurements was calculated following the scheme of Lopez-Zazueta *et al.* (2011) and Ozcan, Meyer & Larsen (2005). They discuss that the main error in calculating spatial derivatives from discrete data arises from truncation errors. We calculated that for our case, the uncertainty is within 12.3 %. Note that the actual error in the measurement is expected to be slightly larger since other non-quantifiable effects (misalignment, secondary flows, etc.) are not accounted for.

2.4. *Elastic characterization of the valve materials*

Tensile tests were conducted to establish the stress–strain relation for the latex, silicon rubber and neoprene used in the construction of the leaflets. A hydraulic piston and a coupled linear variable-differential transformer (LVDT) were employed to exert and measure axial displacements, while a strain-gauge cell arrangement was used to sense the force applied to the specimens. Then, considering an initial equivalent length 29.3 mm for the standard dumbbell-shaped specimens tested in this study, the stress–strain curves were constructed. Each specimen was subjected to a load cycle, elongated up to 45 mm and then released from the load. Tests were conducted at different deformation rates $\dot{\epsilon}$. It was found that the behaviour of all materials was nearly independent of strain rates for $\epsilon < 0.2$ and $\dot{\epsilon} < 10^{-2}$. Hence, the secant modulus of elasticity, E_s, was estimated within these ranges, which is in accordance with the elongation experienced by the leaflets during the experiments.

We have favoured the use of the 'secant' modulus of elasticity over the modulus of elasticity, because the leaflets are rubber-type materials. For such materials, which are often called hyper-elastic, the classical linear relationship between stress and strain may not exist or may be constrained to a very narrow range of strains. In essence E_s

https://doi.org/10.1017/jfm.2013.611 Published online by Cambridge University Press

corresponds to a certain slope on the experimental stress–strain curve for a particular strain interval $[0, \epsilon]$. Thus, for this kind of material the secant modulus provides a reasonable average value of the elastic nature of the material. In this case E_s was obtained for the small strain interval $0 < \epsilon < 0.2$.

The elastic modulus of the composite materials (silicon and aluminium) was obtained by applying the rule of mixtures for unidirectional composites (Bogdanovich & Pastore 1996). The properties of all the tested materials are summarized in table 2.

2.5. *Leakage flow*

In order to prevent the leaflets from getting stuck on the lateral walls of the channel, two lateral thin gaps were included in the design of the experiment. Therefore, the leaflets move without touching the walls allowing adequate PIV and visualization. Each gap has a size of ∼0.5 mm. Clearly, some fraction of the stroke volume goes through these gaps, depending mostly on the average flow rate $\langle \dot{G} \rangle$. In other words, when the hydrodynamic force of the incoming flow is not enough to open the leaflets, some leakage occurs through the gaps. As a result, the volume fraction per stroke that flows between the leaflets is reduced. We found that, in general, the flow rate measurements inferred from the PIV measurements are in good agreement with the average flow rate provided by the pump. Hence, the leakage flow does not affect the main flow significantly. For all cases tested, the leakage flow was found to increase with valve rigidity, but to decrease as the flow rate was increased. A detailed study of the leakage flow can be found in Ledesma-Alonso (2010).

3. Results

3.1. *Valve operation and leaflet deflections*

The motion of the valves was first analysed throughout the systolic and diastolic phases of the cycle. For the flow conditions indicated in table 1, two distinctive situations were identified: (*a*) correct and (*b*) faulty operation of the valve. The sequences of photographs shown in figure 3 portray both situations for the same valve. In the first series of images (figure 3*a*) the deflection process leading to an adequate operation of the valve can be observed. The valve starts opening at $t/T \simeq 0.214$ when the systole begins; then it reaches its maximum aperture and horizontal displacement at $t/T \simeq 0.286$, when the maximum flow rate occurs. The diastolic phase commences at $t/T = 0.429$ and the leaflets move towards a closed position. At $t/T = 0.643$ the valve has completely obstructed the cross-section. During this phase, the negative pressure gradient induces a backward flow. Such a flow exerts a force on the downstream surface of the leaflets and bends them slightly. If this force is below a certain 'critical' bending resistance of the leaflets, an equilibrium state is reached and the valve is restored to its original position at the end of the cycle ($t/T = 1$).

In contrast, a faulty operation of the valve is illustrated by the series of images shown in figure 3(*b*). In this case, the hydrodynamic load on the leaflets is large enough to produce a buckling; hence the leaflets cannot effectively obstruct the channel and prevent the backward flow. As a result, both leaflets move back and forth throughout the operating cycle, and an equilibrium position is not attained because of the remaining bending from the previous cycle. In particular, the buckling process starts when the leaflets make contact at $t/T = 0.571$ (during the diastolic phase) and the forces exerted by the fluid cannot be counterbalanced by the material. Note that the only difference between the two experiments shown above is the frequency of opening. The valve thickness, length and material remain the same.

https://doi.org/10.1017/jfm.2013.611 Published online by Cambridge University Press

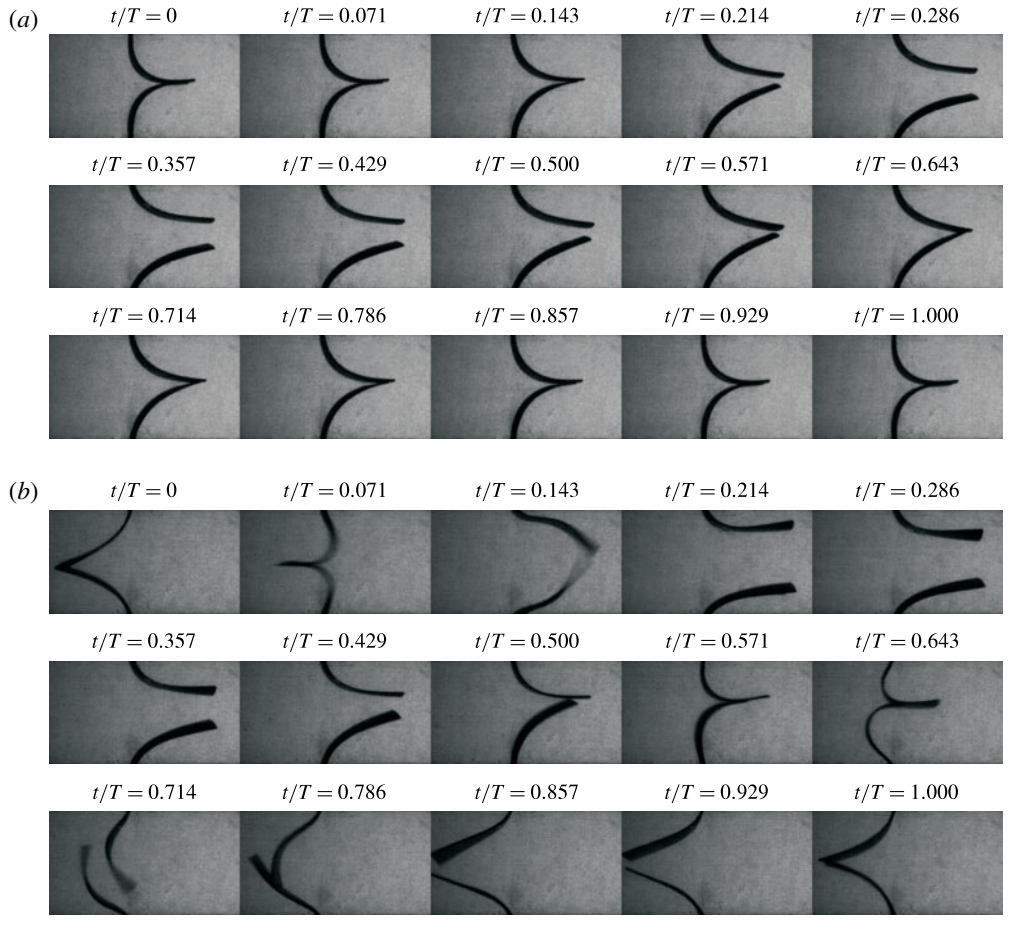


FIGURE 3. Image sequence of valve operation: (*a*) correct operation; (*b*) faulty operation. The case shown corresponds to a leaflet pair made of latex. The leaflet dimensions are $l/h = 1.75$ and $d/h = 0.027$, while the stroke volume is $V = 6 \times 10^{-5}$ m^3 and the frequency is: (*a*) $f = 0.167$ s^{-1} and (*b*) $f = 0.5$ s^{-1}. The main flow is from left to right.

Note that some slight asymmetry between the top and bottom leaflets can be observed, which results from the imperfections of the valve construction and mounting. In fact, the same valve pair could be observed to operate symmetrically or asymmetrically (up or down), if mounted and de-mounted repeatedly. We conducted measurements for both cases, and did not observe significant changes in the performance. The flow is slightly deflected.

The instantaneous positions and elongations of all leaflets were also measured. The leaflet elongation was computed in terms of the instantaneous arclength (a) and the original length of the leaflet (l). The relative deformation can be quantified by

$$\epsilon = \frac{a - l}{l}. \tag{3.1}$$

This expression compares the net elongation of the leaflet with its undeformed length. Significant changes of the elongation were observed to start at around $t/T = 0.15$, when the systolic phase of the cycle begins. Then, the maximum elongation occurs

https://doi.org/10.1017/jfm.2013.611 Published online by Cambridge University Press

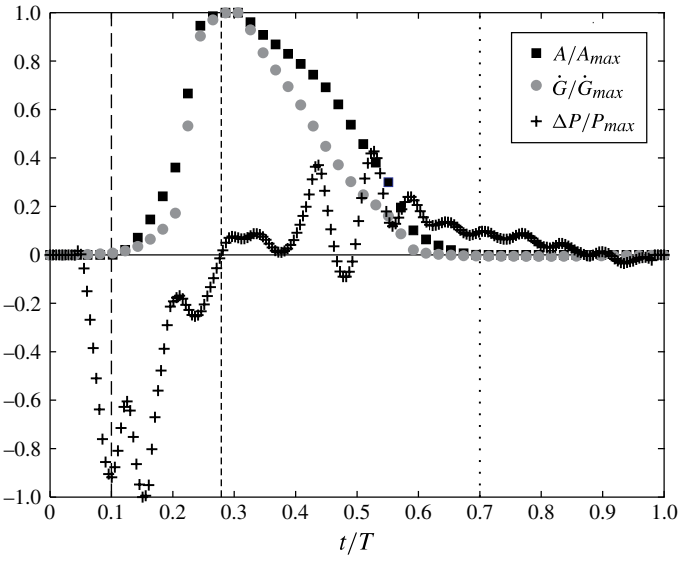


FIGURE 4. Evolution of the opening area, volume flow rate and pressure gradient throughout the average cycle for thin silicone rubber leaflets, $d/h = 0.027$, tested in a flow with a stroke volume $V = 3.8 \times 10^{-5}$ m^3 and a frequency $f = 0.666$ s^{-1}: – – –, valve opening; - - -, maximum opening area and pressure gradient inversion; [· · ·, valve closure.

within the $0.25 < t/T < 0.3$ time interval. Soon after the diastolic phase has commenced ($t/T = 0.45$) a sudden reduction of the elongation follows at $t/T = 0.55$. The valve is completely closed at $t/T \approx 0.65$ and the internal relaxation processes restore the length to the original value for the remaining part of the cycle.

Measurements of the elongation for all the cases studied here are reported elsewhere (Ledesma-Alonso 2010). Most importantly, for all valves, the maximum elongation was never found to be higher than $\epsilon = 0.2$ for all of the materials. Hence, the secant modulus of elasticity can be considered to adequately represent the elastic behaviour of the leaflets.

The size and elastic properties of the leaflets have a direct influence on the maximum aperture area that the valve can produce. Values of the aperture area are plotted in figure 4, along with the flow rate and the pressure, for a typical silicone rubber valve. The corresponding values are normalized with the total cross-section area, the cardiac output and the maximum transvalvular pressure drop. Clearly, the maximum aperture coincides with the maximum flow rate at $t/T = 0.27$. Note also that the relative pressure difference at this particular instant is nearly zero, as expected.

We next investigated the conditions under which the leaflet pair works correctly as a valve. We conducted a large number of experiments varying the geometry (changing l, d and w) and the elastic properties (changing E_s) of the leaflets, as indicated in table 2. We recorded images of the working valve and progressively varied the frequency and displaced volume for a given leaflet pair. For a given displaced volume, the valve works correctly for low frequencies; as this quantity increases, a critical value is reached for which the valve can no longer operate correctly. This condition was identified for all the cases studied. These results are shown in figure 5. Clearly, all valves work correctly for small stroke volumes and frequencies. For a given volume, the valve ceases to operate correctly as the frequency exceeds a certain value. Also, as

https://doi.org/10.1017/jfm.2013.611 Published online by Cambridge University Press

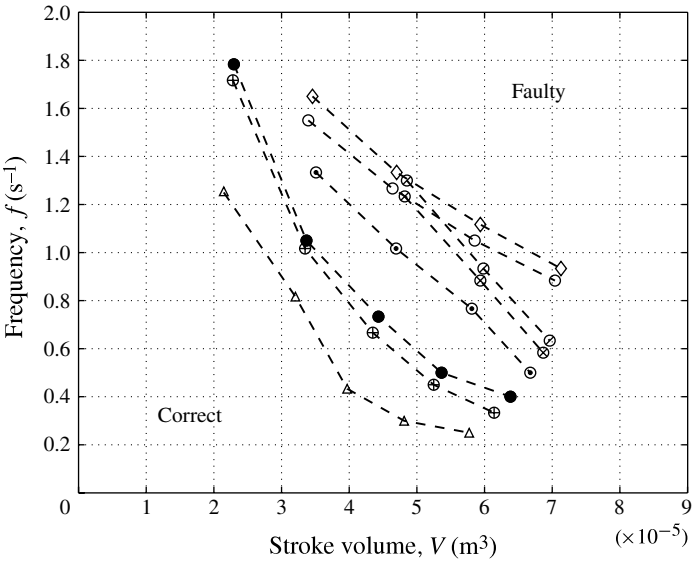


FIGURE 5. Leaflet performance for all flow conditions. Frequency is shown as a function of stroke volume. Each curve represents the behaviour of each leaflet pair. The region below and above each curve represents correct and faulty performance, respectively. Symbols according to table 2.

the stiffness of the valve increases (either by increasing the thickness or the elasticity of the material) the valve operates correctly for a wider range of parameters. From these results we can discard the combination of valve properties for which a correct performance is not observed. A scaling analysis of the results presented here is given in detail in § 4.

3.2. *Velocity fields*

The effect that properties of the leaflets have on the evolution of the flow is not necessarily intuitive. Therefore, assessing the way in which the various parameters affect the stress levels during the operating cycle is a primary objective of the study. Although this objective can be accomplished with the use of the simplified model valve, the corresponding results pertain exclusively to the model valve and cannot be extrapolated to the case of real prosthetic, or native valves. In addition, it must be remarked that native valves and prosthetic devices have three-dimensional shapes that substantially modify their bending behaviour under pulsatile flow conditions.

Now, since the conditions for the correct performance have been identified we can study the flow through valves which operate correctly. The velocity fields were measured downstream and upstream of the valve arrangement. By implementing the phase-locking technique, the phase-average of the velocity field was obtained at specified instants along the cycle. Figure 6 shows the evolution of the velocity field corresponding to a valve with silicone leaflets. When the leaflets open at $t/T = 0.25$ a central jet is formed across the valve. This jet is projected towards a nearly static fluid, thereby inducing a motion directly ahead of the discharge plane. At $t/T = 0.3$, the valve reaches its maximum opening area and a mixing layer is formed creating vortex-like structures. The vortices then separate from their respective leaflet and move downstream.

https://doi.org/10.1017/jfm.2013.611 Published online by Cambridge University Press

https://doi.org/10.1017/jfm.2013.611 Published online by Cambridge University Press

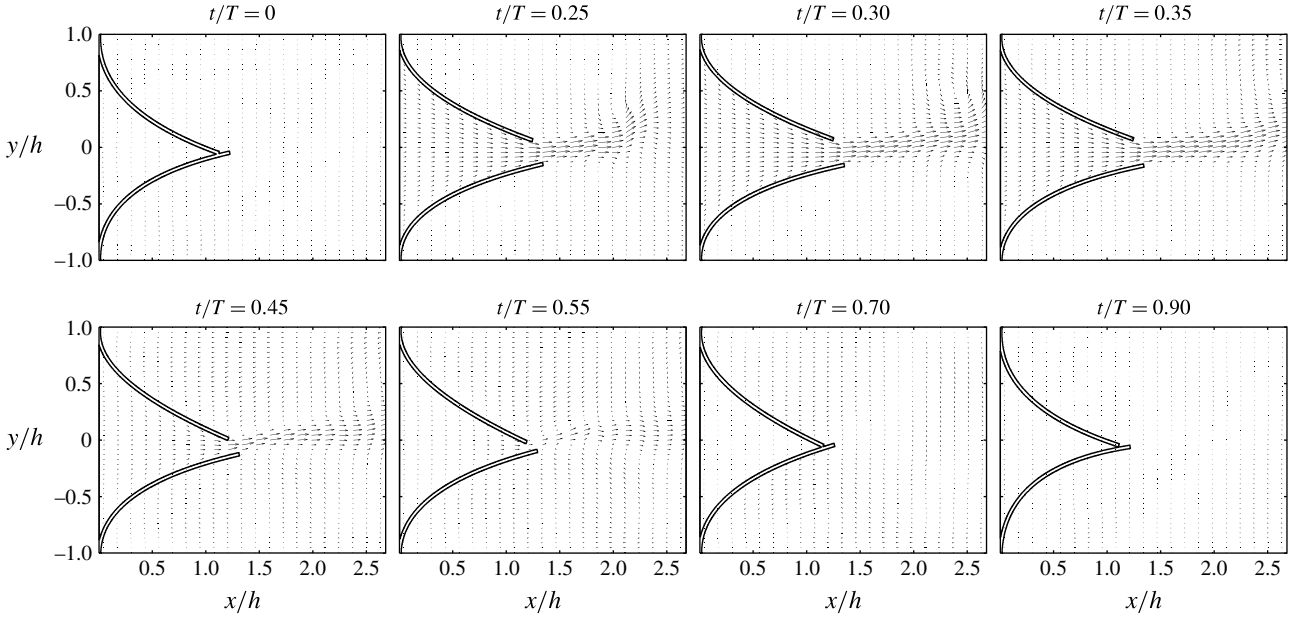


FIGURE 6. Average velocity fields obtained from PIV measurement of the flow across silicone rubber leaflets. The latex leaflet dimensions are $l/h = 1.75$ and $d/h = 0.027$, while the test conditions are $V = 2.6 \times 10^{-5}$ m^3 and $f = 0.333$ s^{-1}. The size of the arrows is proportional to the velocity magnitude.

The valve begins to close, at $t/T \leqslant 0.45$, with reduction of the flow rate. The inertial motion of the fluid in the transvalvular region still produces a noticeable flow through the aperture with its characteristic developed profile. The final closure of the channel takes place at $t/T = 0.7$, with a small remnant backward flow resulting from the diastolic process. Despite having small asymmetries (mainly due to imperfections in the setup) the flow field evolved with a reasonable degree of symmetry. Note that the strain and vorticity fields appear to be continuous across the leaflets. This false artifact is produced by the averaging process. The solid lines in figure 6 depict the average location of the leaflets.

The velocity fields produced by other valves are similar to that shown in figure 6. However, it has been observed that with stiffer leaflets the jet produced becomes narrower and has an increased velocity, while the overall duration of the valve aperture is reduced. It was also observed that valve array became unstable: slight perturbations can induce an asymmetric motion of the leaflets. The resulting flow structures are affected accordingly. The variations of these flow features for different valves are discussed below.

3.3. *Strain rates*

It is well known that blood trauma results, at least partially, from the hydrodynamic stresses (Schneider *et al.* 2007). Fluid stresses are induced in the transvalvular and downstream flow regions. It is important to understand how these fluid stresses are affected by the properties of the leaflets. It is not sufficient to have a valve that correctly opens and closes, preventing backflow; among the possible solutions (see figure 5), those which induce minimal stresses would be preferable because the probability of blood trauma would also be reduced. The simplified flow configuration considered in this study permits us to quantify the change in fluid strain as the elastic and geometric properties of the leaflets are varied. From the velocity fields, that are obtained from the PIV technique, it is possible calculate the fluid strains. It is important to note that there is a significant amount of uncertainty in the reported measurements of strain. The uncertainty is the result of having to calculate spatial derivatives of the velocity field in a finite-spaced domain, as discussed in § 2.3.

The evolution of the magnitude of the rate-of-strain tensor, corresponding to the velocity field shown in figure 6, is shown in figure 7. Before the opening of the valve there is no strain in the flow field, as expected. Then, at $t/T = 0.2$, the valve opens and two low-strain boundary layers begin to develop on the downstream side of the leaflets. Some interaction of the two boundary layers can be observed at the tips of the leaflets. When the valve is about to open fully, at $t/T = 0.3$, the magnitude of the shear in the boundary layers increase substantially. The high-shear region extends from the base (clamped end) of the leaflet to its free edge. Diffusive effects also take place and widen both layers. Moreover, two vortices are initiated at the tips of the leaflets with shear magnitudes in the range $40\ \mathrm{s}^{-1} \leqslant |\boldsymbol{S}| \leqslant 60\ \mathrm{s}^{-1}$ within their cores. For the remaining part of systolic phase ($0.25 \leqslant t/T \leqslant 0.4$) the boundary layers and the vortices continue to move downstream, spreading out into the flow. It is important to note that a high-intensity shearing zone, with values in the range $100\ \mathrm{s}^{-1} \leqslant |\boldsymbol{S}| \sim 125\ \mathrm{s}^{-1}$, is observed in the region formed between the central jet and the surrounding fluid (the highest values being closer to the edges). This region extends around $\Delta x \sim h$ downstream and persists until the valve begins to close again. With the reduction of the flow rate during the diastole ($0.4 \leqslant t/T \leqslant 0.7$), the magnitude of the shear rate decreases, as well as the width and the length of the

https://doi.org/10.1017/jfm.2013.611 Published online by Cambridge University Press

https://doi.org/10.1017/jfm.2013.611 Published online by Cambridge University Press

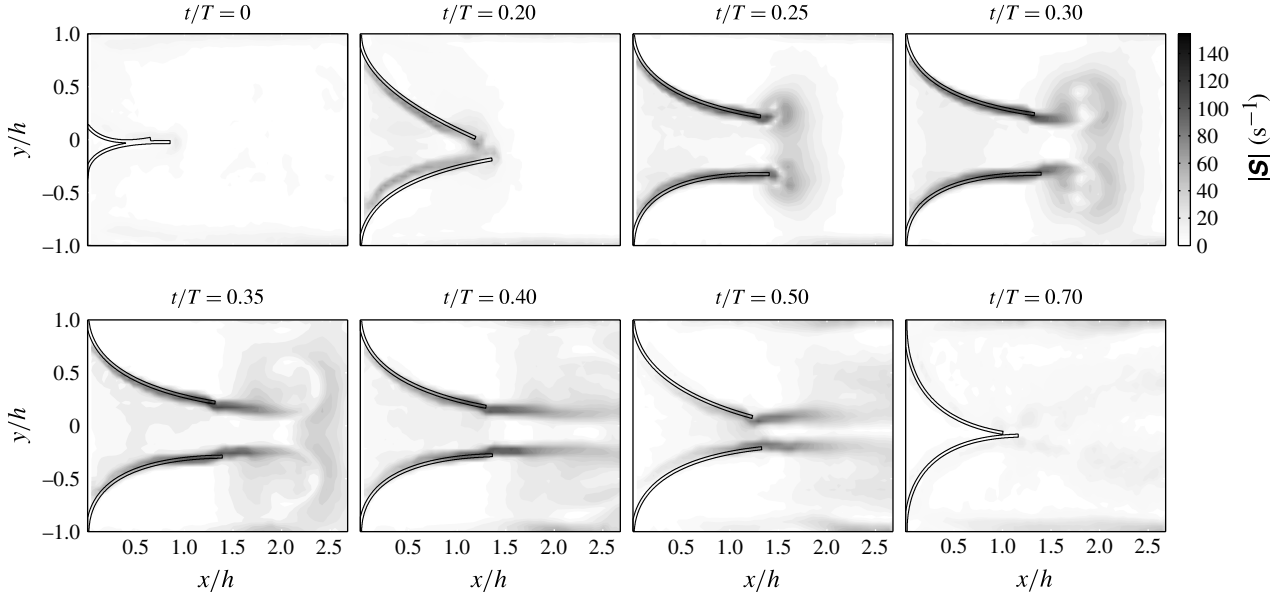


FIGURE 7. Fields of the average magnitude of the strain-rate tensor obtained from PIV measurement of the flow across silicon rubber leaflets. Leaflet dimensions and test conditions are the same as in figure 6. The regions of high strain-rate are shown in dark shades, while regions where the strain-rate is moderate the shading is lighter. For this case, the maximum magnitude of strain-rate is slightly above $|\underline{\underline{S}}|_{max} = 75\ \mathrm{s}^{-1}$'.

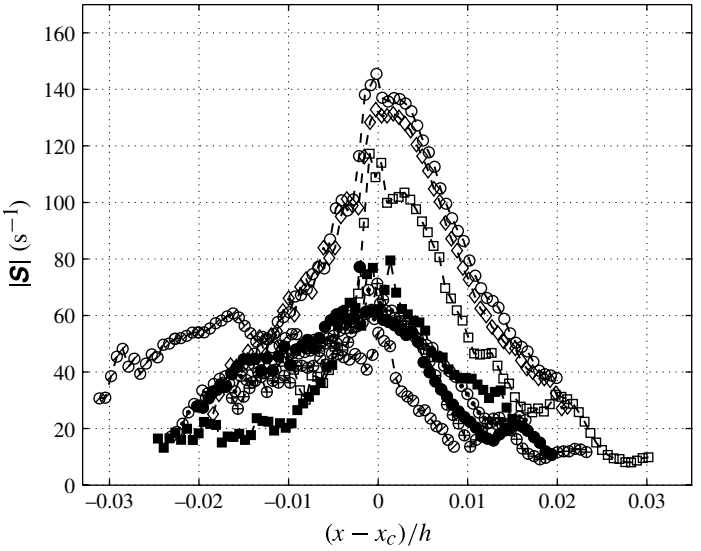


FIGURE 8. Maximum strain rate at every horizontal position $x - x_c$, where x_c is the horizontal position of the free edge of each leaflet. Each curve corresponds to the instant of maximum strain rate for each valve tested, with $V = 3.8 \times 10^{-5}$ m^3 and $f = 0.666$ s^{-1}. Symbols according to table 2.

mixing layers. Upon closure, the remaining eddies dissipate and the shear rate levels become negligibly small.

For the same flow conditions, the maximum strain magnitudes produced by the tested valves are shown in figure 8. Negative values of $(x - x_c)/h$ represent upstream distances with respect to the tip of the leaflet, while positive values indicate the downstream distances. Herein, x_c corresponds to the tip location and $x = 0$ is the clamping position of the leaflets, considering the same reference frame as in figures 6 and 7. It is observed that leaflets with lengths $l/h = 1.5$ and $l/h = 1.75$ produce strain rates which are almost symmetrically located about the edge. Thicker and stiffer leaflets produce significantly higher strain rates, while longer leaflets generate slightly superior values in the upstream zone. In figure 9 an example of the evolution of the maximum strain rate throughout an average cycle is shown. For all the tested valves, the high strain-rate levels are only present during the systolic fraction of the cycle. In general, all the leaflets (thick and thin, stiff and flexible) show the same half-cycle profile. Although only one flow condition is shown, all results have the same qualitative behaviour.

Thin leaflets made of soft materials cause, in general, relatively lower strain-rate levels. On the other hand, thick stiff leaflets generate shear with values up to four times the ones observed for the thin leaflets. Interestingly, the intermediate strain values are generated by much stiffer aluminium-reinforced (or composite) silicone rubber valves. In this case, the bending of the leaflets takes place at the base where a short patch of rubber serves as a hinge. Since no other part of the leaflet is deforming, the reaction produced in the surrounding fluid is reduced somewhat. We can then argue that strain-rate levels are controlled by the bending rigidity (discussed in § 4.2), which is associated with the thickness and the elastic properties of the material, rather than the length of the leaflets.

https://doi.org/10.1017/jfm.2013.611 Published online by Cambridge University Press

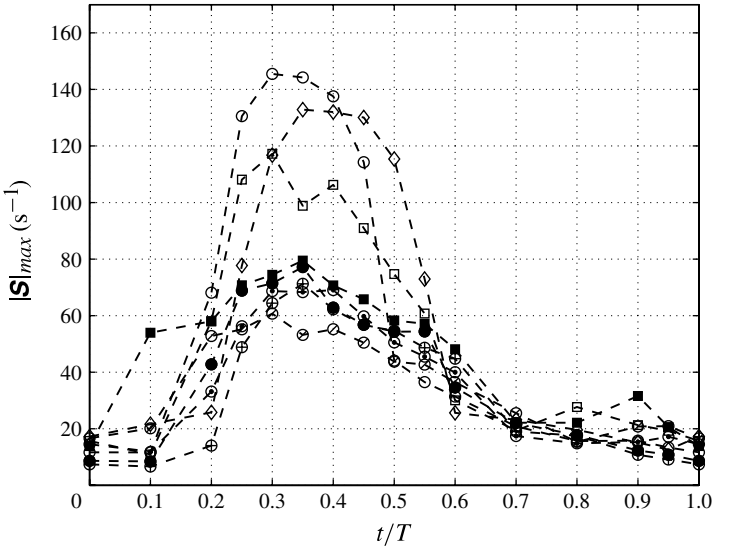


FIGURE 9. Evolution of the maximum magnitude of the strain-rate tensor through the average cycle for all the leaflets, tested in a flow with $V = 3.8 \times 10^{-5}$ m^3 and $f = 0.666$ s^{-1}. Symbols according to table 2. Within these flow conditions, latex leaflets exhibited a defective performance, hence no results of these leaflets are shown here.

4. Discussion

4.1. *Valve performance*

Valve performance can be evaluated in terms of the leaflets' ability to effectively seal the channel. In this sense, a valve preventing a backward flow is considered to perform its function properly (and is faulty otherwise). The valves were tested under the flow conditions indicated in table 1. It is possible to recast these results by considering the main effects that determine the performance of the valve.

During the operation of the valve two main forces can be identified: (i) the elastic force exerted by the leaflets on each other, F_E; and (ii) the hydrodynamic forces of the flow during the diastole, F_H. These forces are depicted in figure 10(*a*). By considering the ratio between these two forces the performance of the valves may be assessed.

In the case of a valve that operates correctly, it is reasonable to assume that the bending moments produced by these forces tend to balance each other until a new equilibrium state is reached. The bending moment produced by the elastic force can be estimated assuming that the leaflets can be treated as slender beams (see figure 10*b*); therefore,

$$F_E \Delta x = E_s I \frac{\mathrm{d}^2 y}{\mathrm{d}x^2}. \tag{4.1}$$

For moderate deflections $\mathrm{d}^2y/\mathrm{d}x^2 \sim l/d^2$, while the moment of inertia for a rectangular cross-section is $I = (wd^3)/12$. Thus, with these considerations, (4.1) can be written as

$$F_E \Delta x \sim \tfrac{1}{12} E_s w l d. \tag{4.2}$$

https://doi.org/10.1017/jfm.2013.611 Published online by Cambridge University Press

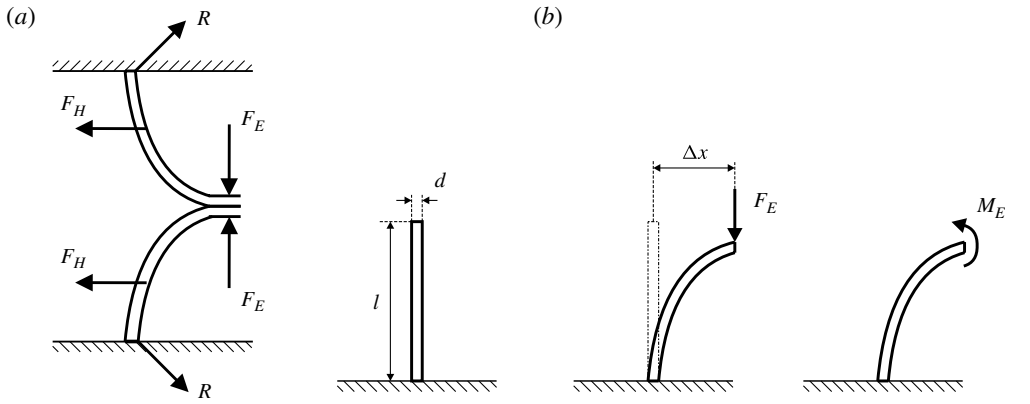


FIGURE 10. Forces acting on the leaflets represented as slender beams: (*a*) balance of hydrodynamic and elastic forces at the equilibrium state; (*b*) elastic force produced by the opposing leaflet and its corresponding bending moment.

On the other hand, the torque produced by the hydrodynamic force can be expressed as

$$F_H h = \tfrac{1}{2}\rho_f A_T h U_D^2, \tag{4.3}$$

where ρ_f is the density of the fluid, U_D is the average velocity during the diastole and A_T is the channel area. The velocity can be expressed in terms of other flow parameters and the size of the channel in the following manner:

$$U_D \simeq \frac{1}{2}\frac{Vf}{t_D h w}. \tag{4.4}$$

The (dimensionless) diastolic fraction appearing in this expression is computed as $t_D = 1 - t_S$ ($t_D = 0.65$, see table 1); the fluid volume, the beating frequency and the channel cross-section are V, f and $A_T = hw$, respectively. As a result, from (4.4) and (4.3), we can write

$$F_H h \sim \frac{1}{8}\frac{\rho_f V^2 f^2}{t_D^2 w}. \tag{4.5}$$

Then, the ratio between the moments given by (4.2) and (4.5) yields

$$\Pi \sim \frac{\rho_f V^2 f^2}{E_s t_D^2 w^2 l d}. \tag{4.6}$$

When Π is below some critical value, Π_c, the moments remain balanced and the valve effectively seals the channel. Otherwise, the leaflets buckle and the valve malfunctions.

Considering the analysis shown above, we can rewrite the two principal variables of the problem, f and V, in appropriate dimensionless terms. The frequency is normalized by considering an equivalent length $d_c = \sqrt{ld}$, and a characteristic elastic speed $U_c = \sqrt{E_s/\rho_s}$. Hence

$$f^* = f\frac{d_c}{U_c}. \tag{4.7}$$

https://doi.org/10.1017/jfm.2013.611 Published online by Cambridge University Press

This quantity compares the flow frequency to the characteristic elastic frequency of the leaflets. A large value of f^* indicates that the flow evolution is faster than the possible elastic response of the material. Hence, a large f^* would most likely result in an incorrect closure of the valve model.

The stroke volume can be written in dimensionless terms by considering the maximum volume of fluid that can flow through the valve when its leaflets are completely opened, that is $2hwl$. Therefore

$$V^* = \frac{V}{2hwl}\frac{h}{d}. \tag{4.8}$$

Written in this form, the ratio d/h appears explicitly, which accounts for the relative thickness of the leaflets. This volume scaling can be interpreted as the relative measure of the available volume of fluid per stroke to the volume of the valve arrangement. Now, considering that the density of the fluid is the same as that of the leaflets, (4.6) can be rewritten as

$$\sqrt{\Pi} \sim kf^*V^*, \tag{4.9}$$

where $k = \sqrt{6}/t_D$ is a constant for a given systolic fraction. Therefore, we can conclude that

$$f^* \sim (V^*)^{-1}. \tag{4.10}$$

All the results of this investigation, recast in dimensionless form according to expressions (4.7) and (4.8), are shown in figure 11. Clearly, all curves conform to the characteristics of a master curve. The regions of correct and faulty performance are clearly separated by this curve. This result is useful to determine if, for a given combination of geometry and elastic properties, a leaflet pair will, or will not, work correctly under certain flow conditions. Note that although the data collapse into a single band of values, some scatter can still be observed. We assumed that the hydrodynamic force was essentially steady; since the flow is, in fact, pulsatile an unsteady force term would also have to be considered to further improve the analysis.

Note that the analysis presented above is limited to the instant at which the valve is about to open or close, which corresponds to a fraction of the flow cycle. For other instants, when the valve is opened, another characteristic velocity would have to be considered. In the next section, a scaling for the fluid strain rate measurements is attempted. Clearly, when there is flow across the valve the analysis presented above is not sufficient.

4.2. *Strain rate*

The strain-rate results, shown in § 3, will be cast in dimensionless form to attempt to gain insight into their scaling properties. The results for the composite valves will not be considered, since their mechanics are less simple and less understood.

As shown in figure 8, thin and soft leaflets cause smaller strain-rate levels than thicker and stiffer leaflets. Also, long leaflets cause higher levels of strain rate at the upstream horizontal position. The width and speed of the exit jet, directly related to the opening area, are significant variables that determine the magnitude of the strain rate. Similarly, the opening area is smaller for leaflets with higher flexural rigidity.

To analyse the strain-rate data, some parameters and dimensionless numbers should be considered. We also need to identify the range of values that these parameters cover for the experiments considered here. First, for the equivalent length of the longitudinal section of a leaflet, d_c, we have $2.99\ \text{mm} \leqslant d_c \leqslant 4.56\ \text{mm}$. The average

https://doi.org/10.1017/jfm.2013.611 Published online by Cambridge University Press

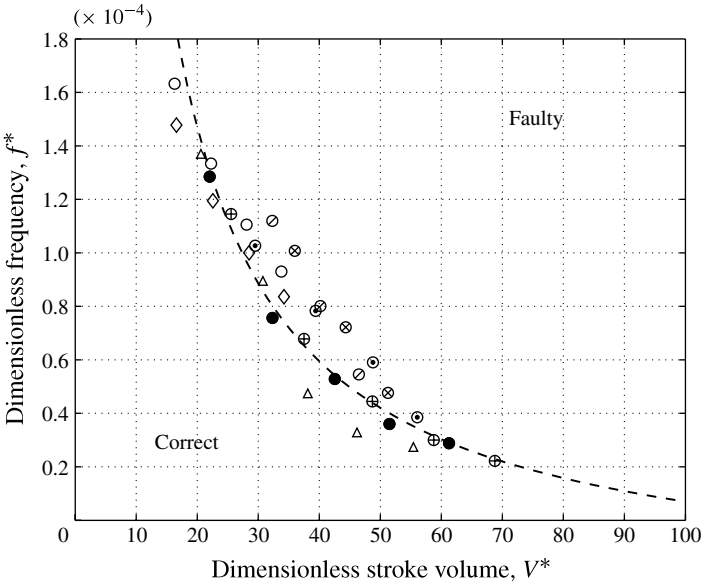


FIGURE 11. Valve performance map. Two distinctive operating regions are identified in the map for any given flow condition (expressed through the frequency, f^*, and the stroke volume, V^*) and any valve type: correctly performing valves would lie in the region labelled 'correct', while the valves performing incorrectly (i.e. prolapsing) would be in the region labelled 'faulty'. Symbols according to table 2.

flow speed during the diastolic phase of the cycle, $U_S = U_D(t_D/t_S)$, is in the range 2.54×10^{-3} m s$^{-1} \leqslant U_S \leqslant 4.31 \times 10^{-2}$ m s^{-1}. The range of the maximum speed, U_{max}, observed within the flow throughout the entire cycle is 1.2×10^{-1} m s$^{-1} \leqslant U_{max} \leqslant 5.1 \times 10^{-1}$ m s^{-1}.

The relevant dimensionless parameters for this problem are: the Reynolds number, the Keulegan–Carpenter and a pseudo-Weissenberg number. The Reynolds number, defined as $Re = (\rho U_S h)/\mu$, has a range of $3.81 \times 10^1 \leqslant Re \leqslant 6.47 \times 10^2$. The Keulegan–Carpenter or period number given by $Kc = (U_S h)/(ldf)$ is in the range $5.49 \times 10^0 \leqslant Kc \leqslant 1.10 \times 10^2$; it compares the hydrodynamic force exerted over the leaflet with its inertia. Finally, the pseudo-Weissenberg number, defined as $Wi^* = (\mu U_S)/(E_s h)$, ranges within $7.69 \times 10^{-11} \leqslant Wi^* \leqslant 2.04 \times 10^{-9}$. This dimensionless parameter is a comparison between the inertia of the flow and the elastic force of the leaflets. Based on the values of these dimensionless numbers, it is reasonable to assume that the problem is dominated by the hydrodynamic forces and the elastic forces of the leaflets (as previously assumed in this section).

A flow field at an arbitrary instant, considering symmetry with respect to the horizontal plane $y = 0$, can be divided into two regions of different morphology. Even though both regions are physically coupled, we can separate the upstream from the downstream region, with respect to the tip of the leaflet (free edge), in order to give different interpretations of their behaviour.

The upstream region can be considered as a plane flow past a curved wall, and the velocity field of this zone resembles that of a boundary layer flow. In this region, the structure of the flow depends on the leaflet properties, in particular on its dimensions. For this region, we can define the dimensionless horizontal position

https://doi.org/10.1017/jfm.2013.611 Published online by Cambridge University Press

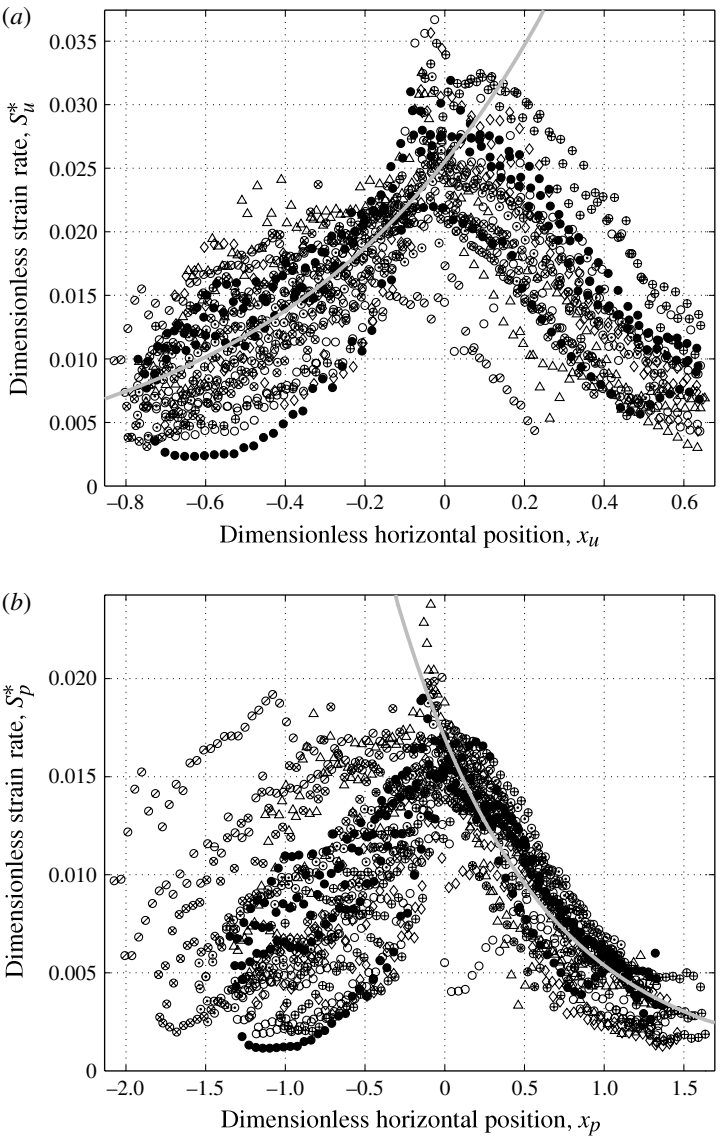


FIGURE 12. Dimensionless strain rate: (*a*) upstream region with respect to the leaflet free edge; (*b*) downstream region with respect to the leaflet free edge. Trend lines correspond to: (*a*) (4.12) and (*b*) (4.14). Symbols according to table 2.

and the dimensionless magnitude of strain rate as

$$x_u = \frac{x - x_c}{l}, \quad S_u^* = \frac{|\boldsymbol{S}|\, d_c}{U_{max}} \left(\frac{h^3}{l^2 d}\right)^{1/2} \left(\frac{Kc}{Re}\right)^{1/4}. \tag{4.11}$$

This choice of S_u^* was found heuristically. Clearly, as shown in figure 12(*a*), the normalized strain-rate measurements fall into a single band of values with less dispersion than that shown in figure 8, for all flow conditions, material properties

https://doi.org/10.1017/jfm.2013.611 Published online by Cambridge University Press

and leaflet geometries. The trend shown in figure 12(*a*) can be fitted to

$$S_u^* = k_3 \exp(k_4 x_u) \tag{4.12}$$

where $k_3 = 0.03$ and $k_4 = 1.56$. Therefore, we can conclude that the strain rate scales with the characteristic strain rate U_{max}/d_c (consistent with a boundary-layer-like behaviour), the square root of the dimensionless thickness d/h and the fourth root of Re/Kc. The strain rate is also proportional to the dimensionless length of the leaflets l/h, which implies that the length of the leaflet is an important parameter for the generation of high strain-rate levels in this flow region.

On the other hand, the downstream zone can be analysed as a two-dimensional free jet emerging in a confined channel. This flow also resembles a time-dependent boundary layer problem, for which the vortex formation at the edge of the leaflets must be considered. The dependence of the flow properties on the leaflet parameters in this region should be as important as their relation in the upstream zone, but the elasticity of the leaflets should be more important in this case. For the downstream zone, we define the dimensionless horizontal position and the dimensionless magnitude of strain rate as

$$x_p = \frac{x - x_c}{h}, \quad S_p^* = \frac{|\boldsymbol{S}|\, d_c}{U_{max}} \left(\frac{h}{d}\right)^{1/2} \left(\frac{Kc\, Wi^*}{Re}\right)^{1/4}. \tag{4.13}$$

Again, S_p^* is found by trial and error. The data, from the downstream region in figure 8, are shown in dimensionless terms in figure 12(*b*). As in the previous case, the dispersion of the data is greatly reduced.

Similarly, the downstream normalized strain rate can be fitted to

$$S_p^* = k_5 \exp\left(k_6 x_p\right) \tag{4.14}$$

where $k_5 = 0.02$ and $k_6 = -1.17$. In this case, we observe that the strain rate varies with the characteristic ratio U_{max}/d_c, the square root of the dimensionless thickness d/h and the fourth root of Re/Kc. The strain rate in the downstream region, in fact, shows the same dependence on the above quantities as the strain rate in the upstream location. Therefore, the key feature of (4.13) is the appearance of the pseudo-Weissenberg number, Wi^*. Here, the strain rate is inversely proportional to the fourth root of Wi^*, which denotes the strong influence of the elastic properties of the leaflets in the downstream region.

From (4.11) and (4.13), we can see that, although the two regions show similar boundary layer features and are affected in a similar manner by the thickness of the leaflets, they show different dependences on the length and the elasticity of the leaflets. Hence, the scaling of the strain rate is not the same for the upstream and downstream regions. Although a precise interpretation of these scalings is missing, this analysis provides some understanding of the main factors that affect the shear generation in this flows. A more in-depth study of the flow is clearly needed.

5. Conclusions

A series of experiments was conducted to study the conditions under which a valve, made of flexible material, fails to prevent a backward flow during the diastolic phase of a cardiac-like cycle. The simplified experimental setup consisted of a quasi-two-dimensional valve arrangement, consisting of rectangular leaflets located at opposite sides of a channel with a rectangular cross-section. Various materials as well as

https://doi.org/10.1017/jfm.2013.611 Published online by Cambridge University Press

different lengths and thicknesses were considered to produce the valve models. The experiments were carried out for a range of frequencies and stroke volumes.

The main objective of the study was to determine how the flow properties, combined with the material properties and the geometrical characteristics of the leaflets, affect the closing performance of the valve. Two relevant quantities were identified: a dimensionless beating frequency and a dimensionless stroke volume. The normalized frequency is a ratio between elastic and flow characteristic times. The dimensionless volume compares the stroke volume with that of the valve. When written in these terms, the results collapse onto a universal curve for which zones of correct and faulty operation can be clearly distinguished. Furthermore, an analysis of the flow through the valves that operated correctly was conducted. In particular, due to its importance in blood damage processes, the strain-rate magnitude was calculated. It was found that flexible leaflets reduce the strain-rate levels, but can only perform properly in a limited range of flow conditions. For instance, very thin (soft) leaflets were observed to become unstable at high flow conditions. In contrast, thick leaflets show a good performance in a wide range of flow conditions but generate, in general, very high strain-rate levels. Also, long leaflets can withstand more severe flow conditions than shorter leaflets, but induce wider regions of large strain-rate levels.

Such elevated shear levels were found to be concentrated within a boundary layer that develops along the curved leaflets, as well as in the free shear layer downstream of the valve. Their specific locations were identified with respect to the free edge of the leaflets. We conducted a dimensional analysis of the flow qualities to shed some light on the process of the hydrodynamic–elastic interaction that occurs during a periodic flow through these model valves. We found that the elastic properties of the leaflets only affect the properties of the downstream flow. Further analysis is required to understand other fundamental aspects of the interactions taking place between the leaflets and the flow, and their impact on the strain rates produced in the flow field.

It is important to conduct a detailed survey of the individual components of the rate-of-strain tensor. Some studies suggest that the elongational components could play major role in the blood damaging process. The type of measurements conducted in this study could be used to evaluate the relative importance of shear over extension rates. Furthermore, the fluctuations of the individual strain components throughout the entire cardiac cycle could also be assessed provided that larger data sets are considered to achieve statically converged data. We plan to pursue such studies in future investigations.

Acknowledgements

The authors wish to acknowledge the financial support from CONACYT-México (grant No. 102527) to conduct this investigation. R.Z. acknowledges the generous support of the M. Moshinsky foundation.

REFERENCES

ALONSO, C., PRIES, A. R. & GAEHTGENS, P. 1993 Time-dependent rhelogical behaviour of blood at low shear in narrow vertical tubes. *Am. J. Physiol. Heart Circ. Physiol.* **265**, H553–H561.

BARSHTEIN, G., WAJNBLUM, D. & YEDGAR, S. 2000 Kinetics of linear rouleaux formation studied by visual monitoring of red cell dynamic organization. *Biophys. J.* **78**, 2470–2474.

BERNACCA, G. M., O'CONNOR, B., WILLIAMS, D. F. & WHEATLEY, D. J. 2002 Hydrodynamic function of polyurethane prosthetic heart valves: influences of Young's modulus and leaflet thickness. *Biomaterials* **23**, 45–50.

https://doi.org/10.1017/jfm.2013.611 Published online by Cambridge University Press

BLUESTEIN, D., RAMBOD, E. & GHARIB, M. 2000 Vortex shedding as a mechanism for free emboli formation in mechanical heart valves. *J. Biomech. Engng* **122**, 125–134.

BOGDANOVICH, A. E. & PASTORE, C. M. 1996 *Mechanics of Textile and Laminated Composites: With Applications to Structural Analysis*. Chapman and Hall.

DIOURTÉ, B., SICHÉ, J. P., COMPARAT, V., BAGUET, J. P. & MALLION, J. M. 1999 Study of arterial blood pressure by a Windkessel-type model: influence of arterial functional properties. *Comput. Meth. Progress Biomed.* **60**, 11–22.

GIERSIEPEN, M., WURZINGER, L. J., OPITZ, R. & REUL, H. 1990 Estimation of shear stress-related blood damage in heart valve protheses – in vitro comparison of 25 aortic valves. *Intl J. Artif. Organs* **13** (5), 300–306.

DE HART, J., PETERS, G. W. M., SCHREURS, P. J. G. & BAAIJENS, F. P. T. 2000 A two-dimensional fluid-structure interaction model of the aortic valve. *J. Biomech.* **33**, 1079–1088.

HELLUMS, D. 1994 1993 Whitaker lecture: biorheology in thrombosis research. *Ann. Biomed. Engng* **22**, 445–455.

HUTCHISON, C., SULLIVAN, P. & ETHIER, C. R. 2011 Measurements of steady flow through a bileaflet mechanical heart valve using stereoscopic PIV. *Med. Biol. Engng Comput.* **49**, 325–335.

JAMIESON, W. R. 2002 Current and advanced prostheses for cardiac valvular replacement and reconstruction surgery. *Surg. Technol. Intl* **10**, 121–149.

LEDESMA-ALONSO, R. 2010 A study of the pulsatile flow and its interaction with rectangular leaflets. Master's thesis, Universidad Nacional Autonoma de Mexico.

LEO, H. L., DASI, L. P., CARBERRY, J., SIMON, H. A. & YOGANATHAN, A. P. 2006 Fluid dynamic assessment of three polymeric heart valves using particle image velocimetry. *Ann. Biomed. Engng* **34**, 936–952.

LIM, W. L., CHEW, Y. T., CHEW, T. C. & LOW, H. T. 2001 Pulsatile flow studies of a porcine bioprosthetic aortic valve in vitro: PIV measurements and shear-induced blood damage. *J. Biomech.* **34**, 1417–1427.

LOPEZ-ZAZUETA, A., LEDESMA-ALONSO, R., GUZMAN, J. E. V. & ZENIT, R. 2011 Study of the velocity and strain fields in the flow through prosthetic heart valves. *Trans. ASME: J. Biomech. Engng* **133**, 10.

OZCAN, O., MEYER, K. E. & LARSEN, P. S. 2005 Measurement of mean rotation and strain-rate tensors by using stereoscopic PIV. *Exp. Fluids* **39**, 771–783.

PALACIOS-MORALES, C. A. & ZENIT, R. 2013 The formation of vortex rings in shear-thinning liquids. *J. Non-Newtonian Fluid Mech.* **194**, 1–13.

PEDRIZZETTI, G. & DOMENICHINI, F. 2006 Flow-driven opening of a valvular leaflet. *J. Fluid Mech.* **569**, 321–330.

POHL, M., WENDT, M. O., WERNER, S., KOCH, B. & LERCHE, D. 1996 In vitro testing of artificial heart valves: comparison between Newtonian and non-Newtonian fluids. *Artif. Organs* **20** (1), 37–46.

PROT, V., SKALLERUD, B. & HOLZAPFEL, A. 2007 Tranversely isotropic membrane shells with application to mitral valve mechanics constitutive modelling and finite element implementation. *Intl J. Numer. Meth. Engng* **71**, 987–1008.

SCHNEIDER, S. W., NUSCHELE, S., WIXFORTH, A., GORZELANNY, C., ALEXANDER-KATZ, A., NETZ, R. R. & SCHNEIDER, M. F. 2007 Shear-induced unfolding triggers adhesion of von Willebrand factor fibres. *Proc. Natl Acad. Sci.* **104** (19), 7899–7903.

SHERWOOD, L. 1997 *Fundamentals of Physiology: A Human Perspective*, 3rd edn. McGraw Hill.

STIJNEN, J. M. A., DE HART, J., BOVENDEERD, P. H. M. & VAN DE VOSSE, F. N. 2004 Evaluation of a fictitious doman method for predicting dynamic response of mechanical heart valves. *J. Fluids Struct.* **19**, 835–850.

WATTON, P. N., LUO, X. Y., WANG, X., BERNACCA, G. M., MOLLOY, P. & WHEATLEY, D. J. 2006 Dynamic modelling of prosthetic chorded mitral valves using the immersed boundary method. *J. Biomech.* **40**, 613–626.

WHITAKER, S. 1981 *Introduction to Fluid Mechanics*. Krieger.

YOGANATHAN, A. P., HE, Z. & CASEY-JONES, S. 2004 Fluid mechanics of heart valves. *Annu. Rev. Biomed. Engng* **6**, 331–362.

https://doi.org/10.1017/jfm.2013.611 Published online by Cambridge University Press